

NEURAL LEVEL SET TOPOLOGY OPTIMIZATION USING UNFITTED FINITE ELEMENTS

CONNOR N. MALLON^{1*}, AARON W. THORNTON², MATTHEW R. HILL^{1,2}, AND SANTIAGO BADIA^{3*}

ABSTRACT. To facilitate widespread adoption of automated engineering design techniques, existing methods must become more efficient and generalizable. In the field of topology optimization, this requires the coupling of modern optimization methods with solvers capable of handling arbitrary problems. In this work, a topology optimization method for general multiphysics problems is presented. We leverage a convolutional neural parameterization of a level set for a description of the geometry and use this in an unfitted finite element method that is differentiable with respect to the level set everywhere in the domain. We construct the parameter to objective map in such a way that the gradient can be computed entirely by automatic differentiation at roughly the cost of an objective function evaluation. The method produces optimized topologies that are similar in performance yet exhibit greater regularity than baseline approaches on standard benchmarks whilst having the ability to solve a more general class of problems, e.g., interface-coupled multiphysics.

1. INTRODUCTION

After the birth of topology optimizations (TOs) in the field of structural design [1], efforts have been made to increase the effectiveness of such automated design approaches and allow for their deployment on a more general class of problems [2,3].

A plethora of TO strategies exist through the literature, the most common of which being density-based methods using the so-called SIMP (Solid isotropic microstructure with penalization for intermediate densities) method [4]. These involve varying a material distribution continuously between 0 and 1 to introduce an artificial representation of the boundary. Although simple for basic structural problems, a way to represent intermediate design variables arising at the boundary must be included, which becomes increasingly complex in multi-physics applications and makes imposing arbitrary boundary conditions non-trivial [5].

An alternative technique that can overcome some of the problems presented by density methods and tackle a more general class of problems (e.g., interface-coupling multiphysics and problems that involve surface PDEs on boundaries) is the level set (LS) TO method [6,7]. Using this approach, the boundary is described by the zero iso-surface of a LS function. It is instead this LS function that is varied to obtain optimized designs. A precise location of the boundary is then available.

A variety of alternative implementations of the LS TO method have been made [8]. They can be distinguished, among other things, by how they update the topology at each iteration and their means of geometry mapping. The methods to update geometries involve either updating the solution of Hamilton-Jacobi equations by a velocity field based on the sensitivity information [9,10] or using a parameterization of the topology that is an explicit function of the design variables of a steepest descent optimization scheme. The latter approach allows one to leverage well-established nonlinear programming techniques and is the method selected for this work. Types of geometry mappings include using the LS function to define a conformal mesh to the boundary, see e.g.

¹ Department of Chemical and Biological Engineering, Monash University, Wellington Rd Clayton, 3800, Victoria, Australia. ² CSIRO, Research Way Clayton, 3168, Victoria, Australia, ³ School of Mathematics, Monash University, Wellington Rd Clayton, 3800, Victoria, Australia. * Corresponding authors E-mails: connor.mallon@monash.edu (Connor Mallon, Department of Chemical and Biological Engineering, Monash University, Wellington Rd Clayton, 3800, Victoria, Australia), santiago.badia@monash.edu (Santiago Badia, School of Mathematics, Monash University, Wellington Rd Clayton, 3800, Victoria, Australia).

[11,12], which requires re-meshing at each iteration, density-based mappings (see e.g. [13–15]), which recover some of the issues related to density methods, or unfitted/immersed boundary techniques (see, e.g., [16–18]). unfitted methods rely on a fixed background mesh and capture the precise location of the boundary in the model using integration on sub-triangulations aligned with the zero iso-surface of the LS function. By doing so, re-meshing and the introduction of intermediate densities are avoided.

A known issue with unfitted techniques is the ill-conditioning problem associated with small cut elements. The common XFEM [19,20] approach uses a finite element (FE) space restricted to the interior domain and cut cells for the solution and requires stabilization in the vicinity of the boundary by, for example, ghost penalty terms [21] or cell aggregation [22,23]. These methods are consistent and can provide high-order approximation [24] however the support of the stabilization terms change depending on the location of the cut cells, leading to potential non-differentiability in the optimization problem which can harm the convergence of gradient-based optimization algorithms. The specific unfitted TO technique used in this work is instead a version of the finite cell method (FCM) [16], in which a non-consistent penalty term is added everywhere in the fictitious domain (outside the physical domain) to provide robustness. This stabilization is suitable for TO because it is differentiable with respect to the level set parameterization (see Section 5). An implementation of the FCM for TO is made in [16], which uses a refined grid for the material boundary compared to the solution to capture fine-scale geometry. We instead use subgrid triangulations using the LS function as in [19] to capture fine-scale structure in the integration and thus avoid the need to increase the number of design variables parameterizing the geometry. The loss of consistency of the FCM is not an issue in TO, where high-order approximations are not very relevant.

It is natural to use a FE function for a discrete representation of the LS. Doing so, a parameterization is obtained with a user-controlled resolution. A common approach to the optimization problem is to take the degrees of freedom (DOFs) of this LS as the design variables [19,25,26]. This choice, however, means that each parameter is only capable of a local influence on the LS function to the surrounding cells. As an alternative, we introduce a neural parameterization of the geometry. We set our design variables in this case to be the parameters of a particular artificial neural network (NN) that outputs the LS function DOFs. Performing this step, we obtain control over the optimization problem by controlling the connectivity of parameters, allowing them to influence cells spread across the domain. Although the expressivity is unchanged, since the LSs are in the same space, the parameters controlling the evolution act to optimize the geometry at multiple scales. The ultimate objective is then for the optimization process to unveil regularized geometries with good performance.

The combination of machine learning and TO was explored as early as the 1990s [27] but has gained massive momentum in recent years [28,29]. NNs and other ML techniques can be incorporated into the TO process in many ways. Common data-driven approaches attempt to train networks to map problem descriptions directly to a geometry [30–33]. These however require pre-training on already optimized samples and suffer from a lack of generalisability [29]. Others replace some or all of the optimization loop for accelerated convergence by training an auxiliary network [34,35]. These approaches are based on the premise, which in general is not necessarily true, that early iterations of the optimization contain the information to produce performant optimal geometries. An alternative method is the inclusion of a NN as an alternative parameterization of the geometry [36–38]. These approaches typically optimize the parameters of a NN representing a continuous function that maps positions in space to a density. These approaches tend to focus on reducing the dimensionality of the design space assuming that NNs can efficiently achieve expressiveness with a small number of parameters [39]. A reduction in parameters does not, however, necessarily lead to faster convergence for NNs [37] compared to the standard SIMP approach.

Instead of focusing on a neural parameterization that reduces the dimensionality of the problem, we select a network description of the geometry which is specifically designed to learn effectively on problems involving the segmentation of a domain. The network used in this case is a modification of

the U-Net convolutional network. The U-Net architecture was originally developed for biomedical image segmentation tasks [40] but has proven successful for a variety of applications in which multi-scale features and spatial correlation is important [41]. These networks are typically composed of encoding and decoding halves. The encoding section maps the context of input images into a low dimensional latent space which is localized in the upsampling section to provide segmentation at the desired resolution. The work in [38] exploited the properties of this network showing improved performance with a U-Net density parameterization for a SIMP structural optimization problem. Similar to [38], we use a trainable input vector for the network and feed this into the up-sampling half of the U-Net. In contrast to most applications of this network, we have no input image and therefore do not need the encoding of half of the network. It is the up-sampling (or decoding) part of the network the one that provides the parameterization of the multi-scale features which are important in this context.

The Julia [42] programming language is used to implement all aspects of this project with the FE toolbox Gridap [43,44] being the main package utilized. We also use the Julia machine learning library Flux [45] for the implementation of the U-Net. Using these foundations, we implement a routine combining NNs with an unfitted FE based TO. The main contributions of this work are the presentation of:

- An unfitted LS TO method with a NN parameterization that assists to achieve simple optimized geometries with similar or better performance compared to baseline methods and
- a fully automatically differentiable unfitted LS TO method for multiphysics problems with complex boundary conditions.

We present the overall framework as follows. First, in Section 2, we present the entire optimization loop at a high level. We then go into more detail about various stages in the loop. Details of the architecture of the neural network are found in Section 3, details of the geometry processing are presented in Section 4, the numerical discretization of the problem is presented in Section 5 and the gradient implementation in Section 6. We then benchmark the method against baseline methods and show the generality of the method with an application to a multiphysics problem with complex boundary conditions in Section 7.

2. OPTIMIZATION PROBLEM

In this section, we provide a succinct overview of the overall TO algorithm proposed in this work. We aim to solve the problem:

$$\begin{aligned} \min_{\mathbf{p}} \quad & J(\mathbf{u}(\mathbf{p}), \mathbf{p}) \\ \text{s.t.} \quad & \mathcal{R}(\mathbf{u}(\mathbf{p}), \mathbf{p}) = 0, \\ & \mathcal{V}(\mathbf{p}) = 0, \end{aligned} \tag{1}$$

where \mathbf{p} are the parameters that describe our geometry, \mathcal{V} is an equality constraint (e.g. for the volume), \mathcal{R} is the PDE residual, \mathbf{u} is the solution of the PDE and J is the objective. If desired, further equality and inequality constraints can then be imposed by adding penalty terms to the objective function.

2.1. Optimization Loop. To optimize the parameters \mathbf{p} , we make use of a gradient-based optimization strategy. To do so, we establish a map between \mathbf{p} and J and a means to compute the gradient $\frac{dJ}{d\mathbf{p}}$ for parameter updates. For the neural LS TO method, \mathbf{p} represents the parameters of a particular NN that outputs a vector ϕ . This vector is processed using the operator \mathcal{H} to obtain the LS ϕ used in the PDE and objective function. It is also only through ϕ that the PDE and objective depend on the parameter vector \mathbf{p} . With these definitions, we present the optimization loop for solving (1) in Figure 1.

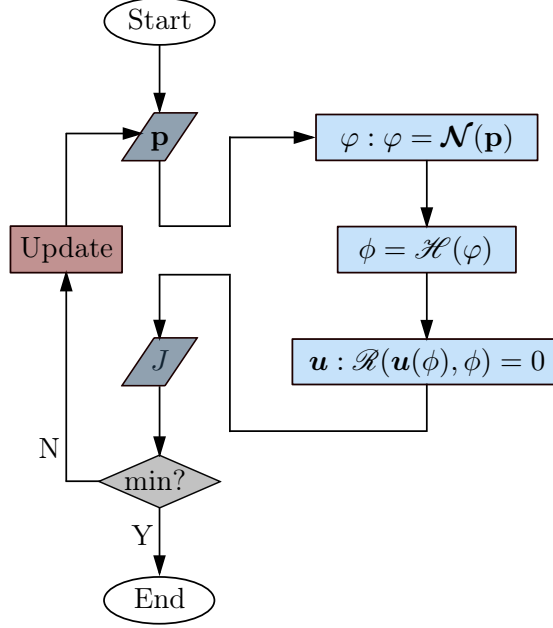


Figure 1. Computational graph of the optimization loop. We start with an input to the system \mathbf{p} , and perform the forward pass by descending through the blue boxes on the right side to obtain a performance measure J as explained in Section 2.1.1. The convergence criteria are used to decide whether this J represents an acceptable minimum. If not, the backward pass is performed to compute an update for the parameters as explained in Section 2.1.2 and the loop is continued.

2.1.1. *Forward Pass.* To solve the forward problem and get a performance measure J for a set of parameters \mathbf{p} we descend through the light blue boxes on the right hand side of Figure 1 by performing the following steps:

- (1) In the first light blue box, we evaluate the network $\mathcal{N} : \mathbf{p} \in \mathbb{R}^{N_p} \mapsto \varphi \in \mathbb{R}^N$, where N_p is the number of parameters and \mathcal{N} is as defined in Section 3.
- (2) In the second light blue box, we process the output of the network φ using the operator $\mathcal{H} : \varphi \in \mathbb{R}^N \mapsto \phi \in V_h^1$ to obtain a suitable LS description of the geometry ϕ , where V_h^1 is the FE space for the LS defined in Section 4. This involves an interpolation on a FE space, smoothing and the inclusion of an equality constraint on the geometry so that the final LS function satisfies $\mathcal{V}(\phi) = 0$. This step is broken down in Section 4. We enforce the equality constraint here to allow for the use of an unconstrained optimization method suitable for NNs.
- (3) In the third light blue box, we solve the FE problem associated with the weak form of the residual $\mathcal{R}(\mathbf{u}_h(\phi), \phi) = 0$ on the domain segmentation defined by ϕ for an approximate solution \mathbf{u}_h obtained using a FE discretization. Details of the FCM used to solve the problem are given in Section 5. We can then evaluate the objective $J(\mathbf{u}_h(\phi), \phi) \in \mathbb{R}$.

2.1.2. *Backwards Pass.* To perform the update for the parameters using a steepest descent optimization strategy, we require an evaluation of the gradient $\frac{\partial J}{\partial \mathbf{p}}$. To do this efficiently at a cost roughly matching that of the forward pass, we use reverse mode differentiation and define rules to propagate sensitivities through each of the steps in the forward pass. We use an adjoint rule for the PDE and use automatic differentiation for all of the partial derivatives, including the derivative of integrals with respect to the LS. The derivative is then passed onto a chosen optimizer to update the parameters \mathbf{p} . The implementation of the gradient computation is discussed in Section 6.

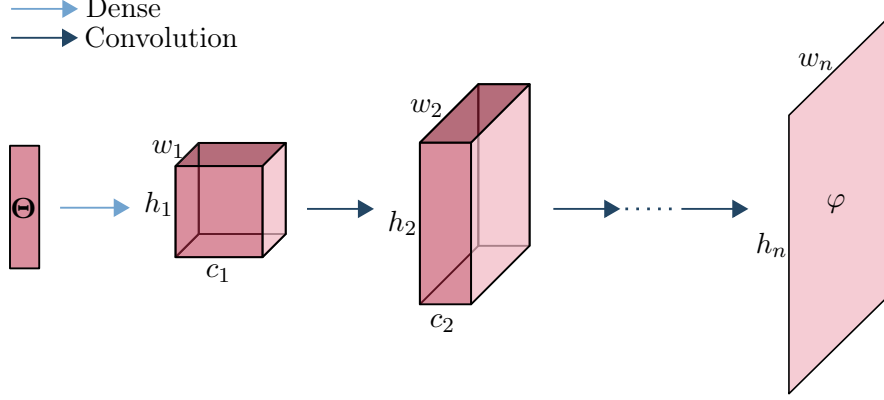


Figure 2. Architecture of the NN. A trainable input vector Θ is fed into the network. The light blue arrow involves a set of operations that include a fully connected layer and the dark blue arrow involves a set of operations that include a convolutional layer. The intermediate data structures are of size (c_l, w_l, h_l) and the final output, after n layers, gives φ .

3. NETWORK ARCHITECTURE

In this section, we present the NN architecture used in the geometry parameterization. This describes the mapping between the parameters \mathbf{p} and the LS vector φ . The network used here is mainly built from convolutional layers. In contrast to a fully connected network, convolutional networks connect smaller sets of neurons in each layer assuming that neurons in close proximity have a more important relationship. This is a natural relaxation for the processing of spatial data. Furthermore, convolutional networks are made efficient by the assumption that features that are found in one local block are likely to be found in a different local block, i.e. somewhere else in the domain. This is done by sharing parameters amongst local blocks in the form of a convolutional filter. The specific architecture used in this work is the one presented in [38]. Because we are simply reparameterizing the pixel values, there is no input into the network in the traditional sense. Most approaches combining NNs and TO use fully connected layers and take the network to provide a map between a spatial input \mathbf{x} and a scalar output $f_\theta(\mathbf{x})$ [36,37]. In our case, we only need a single evaluation of the network to output a vector $f_\theta(\Theta)$ that represents the entire discrete LS function. The input vector in our case is just taken to be a set of trainable parameters Θ .

The architecture of the network is illustrated in Figure 2. The first arrow indicated with the label Dense in Figure 2 contains a fully connected layer and a reshape:

$$\mathbf{x}^{(1)}(\Theta) = \text{reshape}(\mathbf{W}\Theta + \mathbf{b}), \quad \mathbf{x}^1 \in \mathbb{R}^{c_1, w_1, h_1}, \quad (2)$$

where $\mathbf{W} \in \mathbb{R}^{c_1 w_1 h_1, N_\Theta}$ is the dense weight matrix, $\mathbf{b} \in \mathbb{R}^{c_1 w_1 h_1}$ is the bias and $\text{reshape} : \mathbb{R}^{c_1 w_1 h_1} \rightarrow \mathbb{R}^{c_1, w_1, h_1}$ is a reshaping map. The lengths N_Θ , c_1 , w_1 and h_1 represent the length of Θ , the initial number of channels, the latent space image width and the latent space image height, respectively. Note here that the first nonlinearity is imposed at the beginning of the next layer.

The upsampling convolutional layers, depicted by the dark blue arrow in Figure 2, are defined as:

$$\mathbf{x}^{(l+1)}(\mathbf{x}^{(l)}) = \mathcal{P}^{(l)}(\varrho(\Phi^{(l)}(\tanh(\mathbf{x}^{(l)})))), \quad \mathbf{x}^{(l)} \in \mathbb{R}^{c_l, w_l, h_l}, \quad \mathbf{x}^{(l+1)} \in \mathbb{R}^{c_{l+1}, w_{l+1}, h_{l+1}}, \quad (3)$$

where $\Phi^{(l)} : \mathbb{R}^{c_l, w_l, h_l} \rightarrow \mathbb{R}^{c_{l+1}, w_{l+1}, h_{l+1}}$ is a bilinear resize, ϱ is a normalization to a mean of 0 and variance of 1 across the channel dimension and $\mathcal{P}^{(l)} : \mathbb{R}^{c_{l+1}, w_{l+1}, h_{l+1}} \rightarrow \mathbb{R}^{c_{l+1}, w_{l+1}, h_{l+1}}$ is a convolutional operator with kernel size $(5, 5)$.

In this approach, our input to the network Θ is taken to be trainable. So to define our parameter vector \mathbf{p} , we collect the parameters of \mathbf{W} , \mathbf{b} , Θ and \mathbf{P}^i into a vector $\mathbf{p} \in \mathbb{R}^{N_p}$. Then, by

composing the layers, we obtain the function $\mathcal{N} : \mathbf{p} \in \mathbb{R}^{N_p} \mapsto \varphi \in \mathbb{R}^N$:

$$\mathcal{N} = \mathbf{x}^{(n)}(\dots(\mathbf{x}^{(2)}(\mathbf{x}^{(1)}(\boldsymbol{\Theta}))))), \quad (4)$$

where N is the number of DOFs of the FE function for the LS. The output image of size w_n, h_n is interpreted as a vector φ representing the DOFs of the LS FE function as described in Section 4. Importantly, the locality is preserved when defining this function. As we traverse the network, we follow the design principle of the upsampling section of the U-Net and trade-off channel depth for spatial resolution. This means that, in general, the widths w and heights h will increase as we move through the network and the number of channels c will decrease as we move through the network. The exact trade-offs here can vary, but we must set the resizes and channel refinement to ensure $h_n w_n = N$ and $c_n = 1$ so that our output φ makes sense as a vector representing the DOFs for the LS. We can increase the network size in the dense layer by increasing N_{Θ} , w_1 and h_1 and in the convolutional layers by increasing the elements in c and the number of layers.

In a typical LS method, the user is required to manually initialize the geometry with holes. One approach to initializing the NN is to pre-train the network to output the manually selected geometry with holes, as in [46]. Using this as an initial guess, however, causes the geometry to converge quickly to poor local minima. A more common approach when working with NNs and a given objective map is to start with small random weights [47]. In this case, we have high asymmetry in the weights and little activation function saturation. It turns out that a random initialization of the NN with the volume constraint gives an initial guess of a domain with a few holes in random locations. This is in contrast to initializing the LS itself with random values which gives a geometry with many small holes and fine features which is not necessarily desirable [48]. As is common in NN approaches, we can then easily take multiple seeds for the geometry using different random initializations to alleviate initialization dependency. The random initializations simply correspond to different size holes in different locations. Using this method we eliminate the need for manual geometry initialization.

4. LS FUNCTION PROCESSING

In this section, we detail the LS description of the geometry used in the method. We explain how the output vector from the NN φ is used to define the LS to be used in the numerical method. The computation of the LS function is performed in four steps. We introduce an interpolation step in Section 4.1 to obtain a first LS function $\phi_{n(1)}$. In Section 4.2, we smooth out this LS to obtain a smooth LS function $\phi_{f(2)}$. Then, we perform a reinitialization of that LS in Section 4.3 to obtain a LS function $\phi_{s(3)}$. Finally, in Section 4.4, we propose a volume correction strategy to end up with the final LS function $\phi_{b(4)}$. In the subsequent sections, we will refer to this final LS function $\phi_{b(4)}$ as ϕ .

4.1. Interpolation. In this method, we work with discrete LS functions $\phi \in V_h^1$. The DOFs of V_h^1 are the values of the function at the vertices of \mathcal{T}_h , which we denote with $\{\mathbf{x}_i\}_{i=1}^N$, where N is the number of mesh nodes. Thus, there is an isomorphism between V_h^1 and \mathbb{R}^N . The output image vector of the NN φ are the DOFs that uniquely determine the LS FE function.

4.2. Smoothing. Next, we convolve the function with a linear filter for smoothing:

$$\phi_{f(2)i} = \left(\sum_{j=1}^N w_{ij}\right)^{-1} \left(\sum_{j=1}^N w_{ij} \phi_{n(1)j}\right), \quad (5)$$

where $w_{ij} = \max(0, r_f - |x_i - x_j|)$, $\phi_{n(1)j}$ is the j^{th} degree of freedom of the function $\phi_{n(1)}$, $\phi_{f(2)i}$ is the i^{th} degree of freedom of the function $\phi_{f(2)}$ and r_f is the smoothing radius.

4.3. Reinitialization. We then reinitialize the LS as a signed distance function. This is often done to gain control over the spatial gradient of the LS function to improve convergence [8]. In our case, it is of even greater importance as it also guarantees that when we apply the translation to the LS to satisfy the volume constraint, we do not artificially introduce volumes into the domain far from the boundary where the LS is close to zero. This would add discontinuity to the

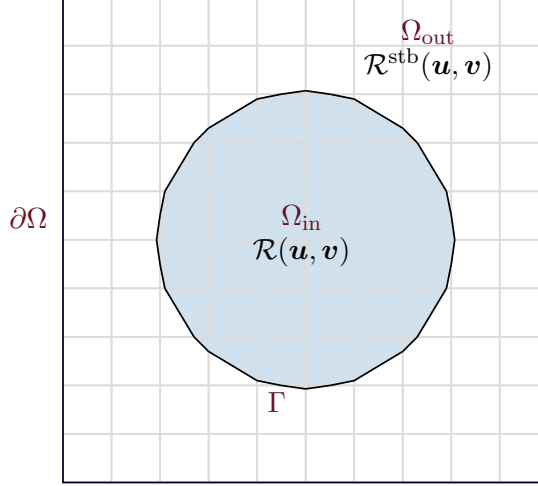


Figure 3. Illustration of the problem domains. The background domain is segmented into the domains Ω_{in} and Ω_{out} . In Ω_{in} , the physical terms $\mathcal{R}(\mathbf{u}, \mathbf{v})$ are integrated. In Ω_{out} , the stabilization terms $\mathcal{R}^{\text{stb}}(\mathbf{u}, \mathbf{v})$ are integrated.

problem harming convergence. To perform this step, we solve the reinitialization equation in [49] to obtain a signed distance function $\phi_{s(3)} \in V_h^1$:

$$\frac{\partial \phi_{s(3)}}{\partial \tau} + \text{sign}(\phi_{s(3)}) (|\nabla \phi_{s(3)}| - 1) = 0. \quad (6)$$

The problem is solved using Picard iterations at steady state using the initial point $\phi_{f(2)}$ so that only one solve of the adjoint equation is required in the backwards pass. Artificial viscosity is added to the problem for stabilization and a surface penalty term is integrated on the embedded boundary to prevent movement of the zero iso-surface in the reinitialization. The weak form of the problem is then to find the solution $\phi_{s(3)} \in V_h^1$ of the equation:

$$\int_{\Omega} (\mathbf{w} \cdot \nabla(\phi_{s(3)})v + c_a h |\mathbf{w}| |\nabla(\phi_{s(3)})| \nabla v - \text{sign}(\phi_{s(3)})v) d\Omega + \int_{\Gamma} (\phi_{s(3)}, v) d\Gamma = 0 \quad (7)$$

for all $v \in V_h^1$, where $\mathbf{w} = \text{sign}(\phi_{s(3)}) (\nabla(\phi_{s(3)}) / |\nabla(\phi_{s(3)})|)$, c_a is the stabilization coefficient, set to 3, and h is the element size.

4.4. Translation. The next task is to impose the volume constraint. This is done by applying a translation to the entire LS function. Here we solve the nonlinear equation \mathcal{V} for the scalar bias b to obtain a translation to the LS function such that the domain Ω_{in} satisfies the volume constraint. A bisection method is used to find the root b of the equation:

$$\mathcal{V} = \int_{\Omega_{\text{in}}} d\Omega - \mathcal{V}_0 = 0, \quad (8)$$

where Ω_{in} is defined by the LS $\phi_{b(4)} = \phi_{s(3)} + b$ and \mathcal{V}_0 is the volume fraction given by the constraint. This is the LS which is then used to define the boundary of the FE problem. Details of how the LS is used to define domains is given in the next Section.

5. NUMERICAL DISCRETIZATION

Here we formulate the numerical discretization of the PDEs being solved in the simulation step of the optimization loop. We consider a background polyhedral bounded domain Ω with boundary $\partial\Omega$. A LS function $\phi(x)$ is used to split Ω into two subdomains $\Omega_{\text{in}}(\phi)$ and $\Omega_{\text{out}}(\phi)$ as follows (see Figure 3):

$$\Omega_{\text{in}}(\phi) = \{x \in \Omega : \phi(x) > 0\}, \quad \Omega_{\text{out}}(\phi) = \{x \in \Omega : \phi(x) < 0\}. \quad (9)$$

We denote the interface between these two subdomains as $\Gamma(\phi) \doteq \partial\Omega_{\text{in}}(\phi) \cap \partial\Omega_{\text{out}}(\phi)$. Let us assume that $\partial\Omega_{\text{in}}(\phi) \cap \partial\Omega \neq \emptyset$. The domain $\Omega_{\text{in}}(\phi)$ is the one in which we consider our PDE problem. The weak form of the continuous problem can be stated as follows: find $\mathbf{u} \in V$ such that

$$\int_{\Omega_{\text{in}}(\phi)} \mathcal{R}(\mathbf{u}, \mathbf{v}) d\Omega = 0, \quad \forall \mathbf{v} \in V. \quad (10)$$

where V is a Hilbert space in which the problem is well-posed. We consider zero flux Neumann boundary conditions on $\partial\Omega_{\text{in}}(\phi) \setminus \partial\Omega$ and (for simplicity) homogeneous boundary conditions on $\partial\Omega_{\text{in}}(\phi) \cap \partial\Omega$; the generalization to non-homogeneous Dirichlet boundary conditions is straightforward.

The domain $\Omega_{\text{in}}(\phi)$ will change along the optimization process. As a result, it is not practical to compute body-fitted unstructured meshes for the geometrical discretization of $\Omega_{\text{in}}(\phi)$. Instead, we consider a background mesh, which can simply be a Cartesian background mesh of Ω and make use of an unfitted FE discretization. Unfitted (or embedded) discretizations relax the geometrical constraints but pose additional challenges to the numerical discretization [21, 50]. The first issue is the integration over cut cells (for details, see [51]). The other issue is the so-called *small cut cell* problem. Cut cells with arbitrary small support lead to ill-conditioned systems [52]. Various techniques can be used to stabilize the problem including the cut finite element method (CutFEM) [21], the aggregated finite element method (AgFEM) [50] and the FCM [53]. We select the FCM method in this case because it is differentiable with respect to the LS everywhere in the domain. The CutFEM and AgFEM are conversely not differentiable.

In order to state the discrete form of the continuous problem, we introduce the unfitted FE space. Let \mathcal{T}_h represent a conforming, quasi-uniform and shape regular partition (mesh) of Ω , h being a characteristic mesh size. Ω can be a trivial geometry, e.g., a square or cube, and \mathcal{T}_h can be a Cartesian mesh. We define a nodal Lagrangian FE space of order $q \geq 1$ on \mathcal{T}_h as:

$$V_h^q = \{\mathbf{v}_h \in \mathcal{C}^0(\Omega) : \mathbf{v}_h|_K \in \mathcal{X}_q(K) \ \forall K \in \mathcal{T}_h\}, \quad (11)$$

where $\mathcal{X}_q(K)$ is the space $\mathcal{Q}_q(K)$ of polynomials with maximum degree q for each variable when \mathcal{T}_h is a quadrilateral or hexahedral mesh and the space $\mathcal{P}_q(K)$ of polynomials of total degree q when \mathcal{T}_h is a simplicial mesh. In this work, we consider low order spaces, which is the most reasonable choice for TO applications.

The weak formulation of the problem solved by the method is now described. Let us represent with $V_{h,0}^q = V_h^q \cap \mathcal{C}_0^0(\bar{\Omega})$ the nodal FE space that vanishes on the boundary $\partial\Omega$.

Now, we can define a first-order FCM discretization of (10) as follows: find $\mathbf{u}_h \in V_h^1$ such that

$$\int_{\Omega_{\text{in}}(\phi)} \mathcal{R}(\mathbf{u}_h, \mathbf{v}_h) d\Omega + \int_{\Omega \setminus \Omega_{\text{in}}(\phi)} \alpha_{\text{out}} \mathcal{R}^{\text{stb}}(\mathbf{u}_h, \mathbf{v}_h) d\Omega = 0, \quad \forall \mathbf{v} \in V_h^1, \quad (12)$$

where $\alpha_{\text{out}} \ll 1$ is the penalty parameter and \mathcal{R}^{stb} is a *stabilizing* differential operator on the artificial domain.

5.1. Poisson Equation. The poisson equation is used to model the temperature $\theta(\mathbf{x})$ that satisfies

$$-\nabla \cdot (\boldsymbol{\kappa} \nabla \theta) = f \quad \text{in } \Omega_{\text{in}}(\phi), \quad (13)$$

where $\boldsymbol{\kappa}$ is the thermal conductivity tensor of the material and f is a thermal source. A zero Dirichlet condition ($\theta = 0$) is prescribed on $\Omega_{\text{in}}(\phi) \cap \partial\Omega$ and a zero flux condition ($\mathbf{n} \cdot (\boldsymbol{\kappa} \nabla \theta) = 0$) is prescribed on $\Gamma(\phi)$.

The FCM approximation of this problem without a source term reads as: find $\theta_h \in V_{h,0}^1$ such that

$$\int_{\Omega_{\text{in}}(\phi)} \boldsymbol{\kappa} \nabla \theta_h \cdot \nabla v_h d\Omega + \int_{\Omega \setminus \Omega_{\text{in}}(\phi)} \alpha_{\text{out}} \boldsymbol{\kappa} \nabla \theta_h \cdot \nabla v_h d\Omega = 0, \quad \forall v_h \in V_{h,0}^1. \quad (14)$$

One can readily check that this method is weakly enforcing the zero flux condition on $\Gamma(\phi)$ as $\alpha_{\text{out}} \rightarrow 0$. We observe that we use the same differential operator in the artificial domain for stabilisation purposes (times the scaling coefficient α_{out}).

We consider the TO problem in which we aim at finding a level-set ϕ that minimizes the integral of the temperature:

$$J(\phi, \theta_h(\phi)) = \int_{\Omega(\phi)} \theta_h(\phi) \, d\Omega, \quad (15)$$

where $\theta_h(\phi)$ is the solution of (14) given ϕ .

5.2. Linear elasticity. We want to obtain the displacement $\mathbf{d}(\mathbf{x})$ that satisfies the linear elasticity equation

$$-\nabla \cdot \boldsymbol{\sigma}(\mathbf{d}) = \mathbf{f} \quad \text{in } \Omega_{\text{in}}(\phi), \quad (16)$$

where $\boldsymbol{\sigma} = \lambda \text{tr}(\boldsymbol{\varepsilon})I + 2\mu\boldsymbol{\varepsilon}$ is the stress tensor, $\boldsymbol{\varepsilon} = \frac{1}{2}(\nabla \mathbf{d} + (\nabla \mathbf{d})^\top)$ is the symmetric gradient, \mathbf{d} is the displacement, λ and μ are the Lamé parameters given by $\lambda = (E\nu)/((1+\nu)(1-2\nu))$ and $\mu = E/(2(1+\nu))$ and \mathbf{f} is the forcing term. A zero Dirichlet condition ($\mathbf{d} = \mathbf{0}$) is prescribed on $\Omega_{\text{in}}(\phi) \cap \partial\Omega$ and a zero stress condition ($\mathbf{n} \cdot \boldsymbol{\sigma}(\mathbf{d}) = 0$) is prescribed on $\Gamma(\phi)$.

The FCM approximation of this problem without a forcing term reads as: find $\mathbf{d}_h \in \mathbf{V}_{h,0}^1 \doteq [V_{h,0}^1]^D$ such that

$$\int_{\Omega_{\text{in}}(\phi)} \boldsymbol{\sigma}(\mathbf{d}_h) : \boldsymbol{\varepsilon}(\mathbf{v}_h) d\Omega + \int_{\Omega \setminus \Omega_{\text{in}}(\phi)} \alpha_{\text{out}} \boldsymbol{\sigma}(\mathbf{d}_h) : \boldsymbol{\varepsilon}(\mathbf{v}_h) d\Omega = 0, \quad \forall \mathbf{v}_h \in \mathbf{V}_{h,0}^1. \quad (17)$$

It is easy to check that the zero-stress condition on $\Gamma(\phi)$ is recovered as $\alpha_{\text{out}} \rightarrow 0$. For the linear elasticity equation, we again use the same differential operator in the artificial domain for stabilisation purposes.

A typical TO problem in solid mechanics is the minimization of the strain energy. In this case, we aim at finding a level-set ϕ that minimizes the cost function

$$J(\phi, \mathbf{d}_h(\phi)) = \int_{\Omega(\phi)} \boldsymbol{\sigma}(\mathbf{d}_h) : \boldsymbol{\varepsilon}(\mathbf{d}_h) \, d\Omega, \quad (18)$$

where $\mathbf{d}_h(\phi)$ is the solution of (17) given ϕ .

5.3. Linear Elasticity with Fluid Forcing Terms. Once again, we want to obtain the displacement $\mathbf{d}_h(\mathbf{x})$ that satisfies the linear elasticity formulation in (16). In this case, however, we consider the surface traction exerted by the fluid:

$$\int_{\Gamma(\phi)} (\mathbf{n} \cdot \nabla \mathbf{u}_h - p_h \mathbf{n}) \cdot \mathbf{v} \, dx, \quad (19)$$

where the fluid velocity \mathbf{u}_h and pressure field p_h are obtained by solving a fluid problem in the domain Ω_{out} . These fields are obtained by solving the Stokes equations with a Brinkmann penalization as in [54] but without intermediate interpolation of permeabilities at the boundary.

In order to approximate the fluid problem, we use a mixed FE method, namely the equal order pair $\mathbf{V}_{h,0}^1 \times V_h^1$.

We find $(\mathbf{u}_h, p_h) \in \mathbf{V}_{h,0}^1 \times V_{h,0}^1$ such that:

$$\begin{aligned} \int_{\Omega} [\alpha \mathbf{u}_h \cdot \boldsymbol{\psi}_h + \mu \nabla \mathbf{u}_h \cdot \nabla \boldsymbol{\psi}_h - p_h (\nabla \cdot \boldsymbol{\psi}_h) - (\nabla \cdot \mathbf{u}_h) q_h - h^2 \nabla p_h \cdot \nabla q_h] \, dx &= 0, \\ \forall \boldsymbol{\psi}_h, q_h \in \mathbf{V}_{h,0}^1 \times V_h^1, \end{aligned} \quad (20)$$

where

$$\begin{cases} \alpha = 0 & \text{in } \Omega_{\text{out}} \\ \alpha = \alpha_u & \text{in } \Omega_{\text{in}} \end{cases} \quad (21)$$

using an artificial porosity α_u to make the fluid problem well posed in the solid domain Ω_{in} and enforce the no-slip boundary condition. In the fluid domain Ω_{out} we recover the Stokes equations.

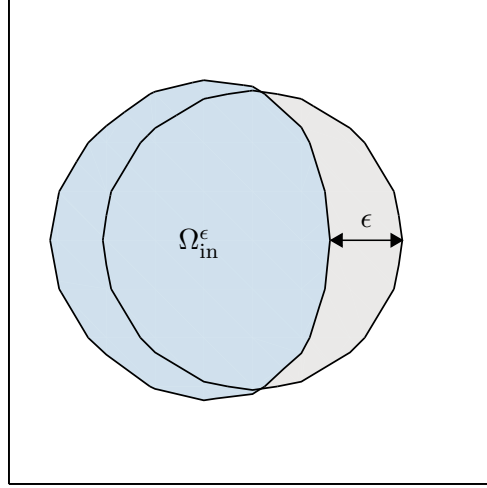


Figure 4. A small perturbation with size ϵ to the LS to form a new domain Ω_{in}^ϵ .

The TO problem once again involves finding a level-set ϕ that minimizes the elastic strain using (18).

5.4. Differentiability of the unfitted FE solver. An important property for the convergence of a TO strategy is the notion of shape differentiability of the cost function. A functional under a PDE constraint is considered shape differentiable if the mapping $\phi \rightarrow J(\mathbf{u}_h(\phi), \phi)$ is differentiable at the admissible set of domains in Ω defined by ϕ . In this section, we discuss how the choice of FE stabilization can effect this property.

The model problem in (14) with a FCM stabilization is equivalent to that of a typical two phase conductivity problem. With a solution $\mathbf{u}_h \in H^1(\Omega)$, the functional $J(\mathbf{u}_h, \phi)$ for this problem can be proven to be shape differentiable, see [55, Theorem 4.9].

Conversely, unfitted techniques involving stabilization only in the vicinity of the boundary are in general not shape differentiable. Regions of non differentiability arise (typically when the boundary crosses over mesh nodes) harming the convergence of the geometry to optimized solutions [56]. To see why this is the case, we investigate shape perturbations under the CutFEM and AgFEM formulations.

If we were to use a restricted space for the solution and add ghost penalty terms in the vicinity of the interface following the CutFEM method [57], the problem is to find $u_h \in W_{h,0}^1$ such that:

$$\int_{\Omega_{in}(\phi)} \mathcal{R}(\mathbf{u}_h, \mathbf{v}_h) d\Omega_{\Omega_{in}} + j(\mathbf{u}_h, \mathbf{v}_h)_{\Gamma_G} = 0, \quad \forall \mathbf{v}_h \in W_{h,0}^1, \quad (22)$$

for a ghost penalty term j on a ghost skeleton triangulation Γ_G using the space $W_{h,0}^1$ as in [57]. Consider the change to the domain Ω_{in} from Figure 3 caused by a perturbation $\epsilon\delta$, where $\epsilon \in \mathbb{R}$ and $\delta \in V_h^1$, to the LS function ϕ . The resulting domain Ω_{in}^ϵ may be as in Figure 4. The ghost penalty term in this formulation does not depend on ϵ and instead changes depending on which cells are cut. Specifically, if Γ^ϵ crosses over a mesh node as in Figure 5, the ghost skeleton triangulation includes the faces of a new element. Non-zero terms are integrated on this triangulation introducing discontinuity to the problem with respect to the shape, since:

$$\lim_{\epsilon \rightarrow 0} [j(\mathbf{u}_h, \mathbf{v}_h)_{\Gamma_G^\epsilon} - j(\mathbf{u}_h, \mathbf{v}_h)_{\Gamma_G}] \neq 0. \quad (23)$$

With different terms added to the linear system which do not go to zero with ϵ , we can see that the derivative of the solutions with respect to the shape can be ill-defined. A cost function operating on the solution could not, in general, be shape differentiable at these points.

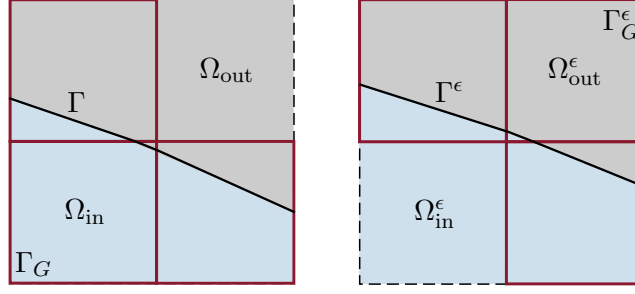


Figure 5. The change in a portion of the ghost skeleton triangulation Γ_G , depicted by the red faces, before and after a perturbation to the boundary.

In the AgFEM, the problem is to find $u_h \in V_{h,0}^{agg}$ such that:

$$\mathcal{R}(\mathcal{E}(\mathbf{u}_h), \mathcal{E}(\mathbf{v}_h))_{\Omega_{in}} \quad \forall v_h \in V_{h,0}^{agg}, \quad (24)$$

for the extension operator \mathcal{E} and space $V_{h,0}^{agg}$ as defined in [50]. Similar to the CutFEM, regions of non-differentiability in the problem exist when the zero isosurface of the LS crosses over mesh nodes:

$$\lim_{\epsilon \rightarrow 0} [\mathcal{R}(\mathcal{E}(\mathbf{u}_h), \mathcal{E}(\mathbf{v}_h))_{\Omega_{in}} - \mathcal{R}(\mathcal{E}^\epsilon(\mathbf{u}_h), \mathcal{E}(\mathbf{v}_h))_{\Omega_{in}^\epsilon}] \neq 0, \quad (25)$$

since $\mathcal{E}^\epsilon(\mathbf{u}) \neq \mathcal{E}(\mathbf{u}_h)$ in general because the support for cut cells potentially changes depending on which cells are cut. Following the same reasoning as above, the method is therefore not shape differentiable. The same is true for other methods which use stabilization approaches that act only in the vicinity of cut cells, e.g. [58], using similar branching strategies when crossing a node or reaching a certain threshold. \square

6. GRADIENT IMPLEMENTATION

To the best of our knowledge, there is no existing implementation of an unfitted LS TO method that accepts arbitrary residuals defining the PDE and computes the entire gradient $\frac{dJ}{d\mathbf{p}}$ by automatic differentiation. Making use of a backwards pass, we do this efficiently by defining differentiation rules for each of the steps in the method.

6.1. Integral Differentiation Operator. The backward pass is mainly composed of gradients of integrals with respect to the DOFs of FE functions. To make the derivative computation efficient, we exploit the fact that the DOFs only have an effect on surrounding cells and utilize the optimizations exploiting sparsity in the FE library Gridap [59]. Integrals in the domain can be divided into cell-wise components:

$$\mathcal{J}(\mathbf{u}, \mathbf{v}, \phi) = \sum_{K \in \mathcal{T}_h} \mathcal{J}^K(\mathbf{u}^K, \mathbf{v}^K, \phi^K), \quad (26)$$

where $\mathbf{u}^K \in \mathbb{R}^{\Sigma_u}$, $\mathbf{v}^K \in \mathbb{R}^{\Sigma_v}$ and $\phi^K \in \mathbb{R}^{\Sigma_\phi}$ are the DOFs parameterising the restrictions of u, v and ϕ to the cell K and Σ_u, Σ_v and Σ_ϕ are the number of DOFs in K for the respective functions. Gradients can then be computed at roughly the cost of an integral evaluation for each cell K :

$$\frac{\partial \mathcal{J}^K}{\partial \phi} = \nabla_\phi^F \mathcal{J}^K(\mathbf{u}^K, \mathbf{v}^K, \phi^K), \quad (27)$$

where the operator ∇_ϕ^F represents taking the gradient with respect to ϕ^K using a vectorized forward propagation of dual numbers [60]. To make taking derivatives in this way possible for the LS, we implement the integrals so that each ϕ^K is accepted as the argument to compute the contribution \mathcal{J}^K :

$$\mathcal{J}^K : \phi^K \in \mathbb{R}^{\Sigma_\phi} \mapsto \mathcal{J}_K(\mathbf{u}^K, \mathbf{v}^K, \phi^K) \in \mathbb{R}. \quad (28)$$

where

$$\mathcal{J}^K(\mathbf{u}^K, \mathbf{v}^K, \phi^K) = \int_{K(\phi^K)} \mathcal{I}(\mathbf{u}^K, \mathbf{v}^K) dK \quad (29)$$

A key point is that the integral function subroutines, including all the unfitted FE tools, are implemented in such a way as to allow the propagation of dual numbers through the code. We also make use of a reverse mode operator ∇^R for the backwards propagation of derivatives used where appropriate, e.g., for the NN.

6.2. Backwards Pass Routine. We now present the backwards pass in detail. To compute the sensitivity of the objective with respect to the parameters, we start with the seed $\frac{dJ}{dJ} = 1$ and propagate derivatives in reverse mode using the chain rule:

$$\frac{dJ}{d\mathbf{p}} = \frac{dJ}{dJ} \left(\frac{\partial J}{\partial \phi} + \frac{\partial J}{\partial \mathbf{u}} \frac{d\mathbf{u}}{d\phi} \right) \frac{d\phi}{d\varphi} \frac{d\varphi}{d\mathbf{p}} \quad (30)$$

where an adjoint method on the problem residual \mathcal{R} is used to differentiate through the PDE:

$$\frac{\partial J}{\partial \mathbf{u}} \frac{d\mathbf{u}}{d\phi} = -\lambda^T \frac{d\mathcal{R}}{d\phi} \quad (\text{here we solved } \frac{d\mathcal{R}^T}{d\mathbf{u}} \lambda = \frac{dJ^T}{d\mathbf{u}}). \quad (31)$$

We then use the chain rule to differentiate through the LS function processing steps:

$$\frac{d\phi}{d\varphi} = \frac{d\phi}{d\phi_{s(3)}} \frac{d\phi_{s(3)}}{d\phi_{f(2)}} \frac{d\phi_{f(2)}}{d\varphi}. \quad (32)$$

The volume constraint here involved a root finding method. To differentiate through this step, we utilize the implicit function theorem:

$$\frac{d\phi}{d\phi_{s(3)}} = \frac{\partial \phi}{\partial \phi_{s(3)}} - \frac{\partial \phi}{\partial b} \frac{\partial \mathcal{V}^{-1}}{\partial b} \frac{\partial \mathcal{V}}{\partial \phi_{s(3)}}, \quad (33)$$

and to differentiate through the signed distance map, we use the adjoint method once again for the residual \mathcal{R}_s equal to the integral in (7). Finally, we use standard backpropagation to compute the derivative with respect to the parameters of the NN. The steps of the backward pass are presented explicitly in Algorithm 1.

7. NUMERICAL EXPERIMENTS

7.1. Benchmark Results. We first compare the optimized results obtained for benchmark problems against baseline methods using the model problems presented in Section 5.

The method presented in this work, the NN-LS method, is compared against its non-neural counterpart the Pixel LS (Pixel-LS) method, that is, the same method without a neural prior where instead the DOFs of the LS function are taken as the optimization parameters. We also compare the method against the SIMP method of TO again using both a neural prior (NN-SIMP) and the standard approach (Pixel-SIMP). Following a standard SIMP implementation of the heat conduction problem, we use a conductivity based on the power law $k = \alpha_T + (1 - \alpha_T)\rho^\gamma$ where ρ is a design variable given by a FE function constructed on the space V_h^1 where the DOFs are the optimization parameters or output vector of the NN in the Pixel-SIMP and NN-SIMP cases, respectively, and γ is the penalization parameter, taken to be equal to 3. Similarly, for the SIMP implementation of the structural problem, we use a Youngs Modulus $E = \alpha_d + (1 - \alpha_d)\rho^\gamma$. To maintain a fair comparison between methods, we use the optimizers most widely regarded as suitable for the particular parameterization. Namely, we take the most commonly used MMA optimization strategy [61] for the pixel parameterization and the ADAM strategy [62] for the NN.

7.1.1. Benchmark Problems. The first problem studied is the poisson equation to model heat conduction with the setup in Figure 6a selected from [63]. For this problem, we set $k_0 = 1m^2s^{-1}$, $\alpha_T = 0.01$, $f = 0.01Ks^{-1}$, use homogenous Dirichlet and Neumann conditions and use a mesh of 95×95 with a 0.4 volume fraction. For the NN, we set the number of convolutional layers to 5, $N_\Theta = 64$, $w = (12, 12, 24, 46, 96, 96)$, $l = (12, 12, 24, 46, 96, 96)$ and $c = (16, 128, 64, 32, 16, 1)$.

The second problem studied is the typical MBB problem described in [4] with the setup as in Figure 6b. For this problem, we set $\nu = 0.3$, $E = 1Pa$, $\alpha_d = 0.001$ and $F = 1N$ and use a mesh of 287×95 with a 0.4 volume fraction. We use the same network as in the poisson problem but set $w = (36, 36, 64, 128, 256, 256)$

Algorithm 1 Backwards Pass

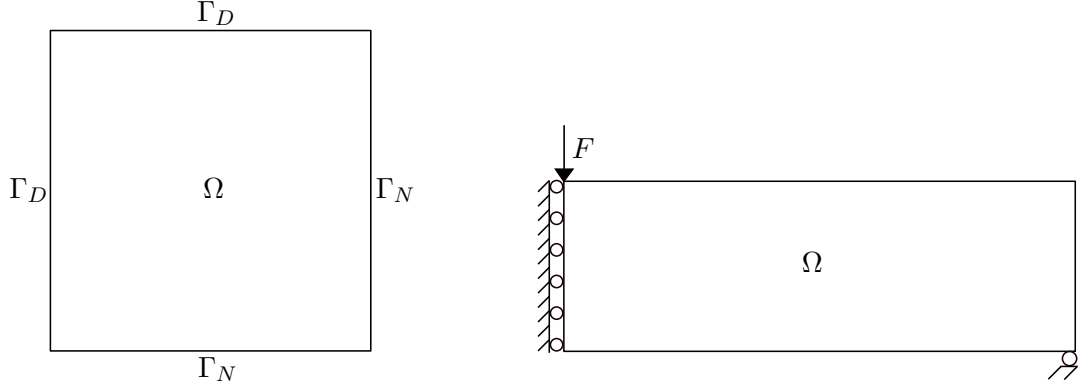
```

Initialize  $\frac{dJ}{dJ} \leftarrow 1$ 
Extract  $\phi^K \in \mathbb{R}^{\Sigma\phi}$ ,  $\mathbf{u}^K \in \mathbb{R}^{\Sigma u}$  from  $\phi, \mathbf{u} \forall K \in \mathcal{T}_h$ .
for  $K \in \mathcal{T}_h$  do
     $\frac{\partial J^K}{\partial \mathbf{u}} \leftarrow \nabla_u^F J(\mathbf{u}^K, \phi^K)$ 
     $\frac{\partial J^K}{\partial \phi} \leftarrow \nabla_\phi^F J(\mathbf{u}^K, \phi^K)$ 
end for
Assemble the gradients  $\frac{\partial J}{\partial \mathbf{u}} \in \mathbb{R}^{N_u}$  and  $\frac{\partial J}{\partial \phi} \in \mathbb{R}^N$ 
Assemble the sparse jacobian associated with the residual  $\frac{\partial \mathcal{R}}{\partial \mathbf{u}} \in \mathbb{R}^{N_u, N_u}$ 
Solve the adjoint equation  $\frac{\partial \mathcal{R}}{\partial \mathbf{u}} \lambda = \frac{\partial J}{\partial \mathbf{u}}$  for  $\lambda \in \mathbb{R}^{N_u}$ 
Extract  $\lambda^K \in \mathbb{R}^{\Sigma u}$  from  $\lambda \forall K \in \mathcal{T}_h$ 
for  $K \in \mathcal{T}_h$  do
     $\frac{\partial J}{\partial \mathbf{u}} \frac{\partial \mathbf{u}^K}{\partial \phi} \leftarrow \nabla_u^F \mathcal{R}(\mathbf{u}^K, \lambda^K, \phi^K)$ 
end for
Assemble the gradient  $\frac{\partial J}{\partial \mathbf{u}} \frac{\partial \mathbf{u}}{\partial \phi} \in \mathbb{R}^N$ 
 $\frac{dJ}{d\phi} \leftarrow \frac{\partial J}{\partial \phi} + \frac{\partial J}{\partial \mathbf{u}} \frac{\partial \mathbf{u}}{\partial \phi}$ 
Compute the vector-jacobian-products:
 $\frac{\partial J}{\partial b} \leftarrow \frac{dJ}{d\phi} \nabla_b^R \phi(\phi_{s(3)}, b)$ 
 $\frac{\partial J}{\partial \phi} \leftarrow \frac{dJ}{d\phi} \nabla_\phi^R \phi(\phi_{s(3)}, b)$ 
Compute the gradients:
 $\frac{\partial V}{\partial \phi} \leftarrow \nabla_u^R V(\phi_{s(3)}, b)$ 
 $\frac{\partial V}{\partial b} \leftarrow \nabla_u^F V(\phi_{s(3)}, b)$ 
 $\frac{dJ}{d\phi_{s(3)}} \leftarrow \frac{\partial J}{\partial \phi_{s(3)}} - \frac{\partial J}{\partial b} \frac{\partial \psi}{\partial b}^{-1} \frac{\partial \psi}{\partial \phi_{s(3)}}$ 
Assemble the sparse jacobian associated with the residual  $\frac{\partial \mathcal{R}_s}{\partial \phi_{s(3)}} \in \mathbb{R}^{N, N}$ 
Solve the adjoint equation  $\frac{\partial \mathcal{R}_s}{\partial \phi_{s(3)}} \lambda_s = \frac{\partial J}{\partial \phi_{s(3)}}$  for  $\lambda_s \in \mathbb{R}^N$ 
for  $K \in \mathcal{T}_h$  do
     $\frac{d\mathcal{R}_s}{d\phi_{f(2)}}^K \leftarrow \nabla_{\phi_{f(2)}}^F \mathcal{R}_s(\phi_{s(3)}^K, \lambda_s^K, \phi_{f(2)}^K)$ 
end for
Assemble the gradient  $\frac{dJ}{d\phi_{f(2)}} \in \mathbb{R}^N$ 
Compute the vector-jacobian-products:
 $\frac{dJ}{d\varphi} \leftarrow \frac{dJ}{d\phi_{f(2)}} \nabla_\varphi^R (\phi_{f(2)}(\varphi))$ 
 $\frac{dJ}{dp} \leftarrow \frac{dJ}{d\varphi} \nabla_p^R (N(\mathbf{p}))$ 

```

7.1.2. Optimized Structures. To compare the SIMP and LS results, the optimized density is converted to a LS by taking the 0.5 isosurface of the density and recomputing the objective function value.

The optimized geometries using the various methods are seen in Figure 7. In all cases, the neural parameterization results in more regular geometries. The pixel-based methods could be regularized by augmenting the objective function with a penalization term although this would require manual tuning of a penalization parameter and may have an impact on the convergence. Simplistic structures could also be obtained for the pixel-based cases by controlling the filter radius and mesh resolution although this would prevent fine-scale structure. The NN-LS method instead allows for fine-scale features resolved in the final layer of the network but still produces performant regular geometries as the multi-scale influence of the parameters in the neural parameterization encourages globally performant structures to emerge. The use of the NN is also seen to suppress numerical artifacts observed in the pixel-LS solutions. For the MBB problem, the compliance measurements for all methods fall within a few percent of each other. For the heat conduction problem, however, the NN-LS method has the best performance by a fair amount followed by



(a) Heat conduction problem setup. The top and left sides Γ_D are given a Dirichlet condition and the bottom and right sides Γ_N are given a Neumann condition.

(b) The right half of the MBB problem exploiting symmetry. The roller supports provide vertical restraint on the left-hand side and horizontal restraint in the bottom right corner. A downward force F is prescribed on the top left corner.

Figure 6. Benchmark problems

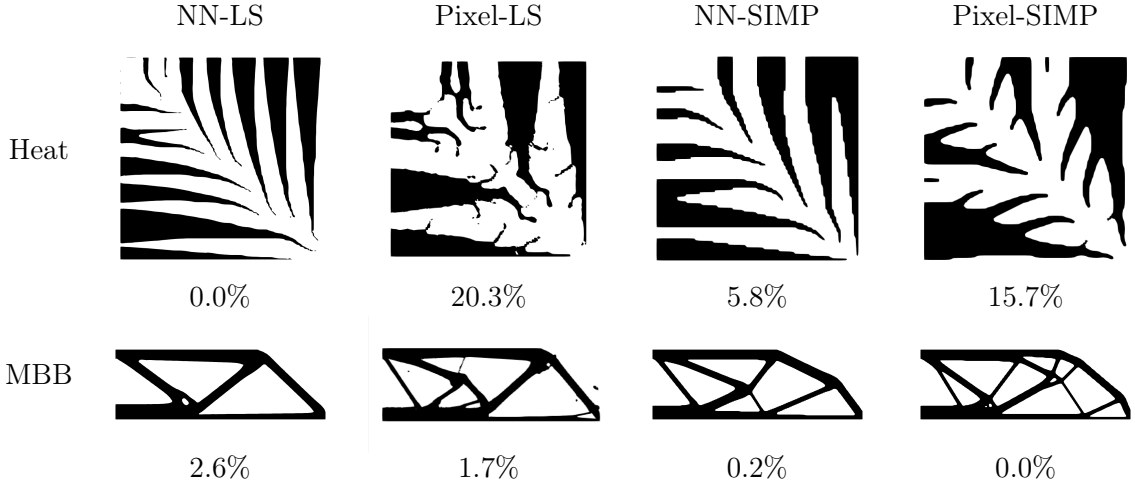


Figure 7. Optimized geometries for the various methods. The percentage under each geometry represents its performance relative to the best performing geometry in the row as measured by the objective function.

the NN-SIMP baseline. The regular geometries produced by the NNs in these cases outperform their pixel counterparts by a significant amount in both the LS and SIMP cases. The U-Net here seems able to find better minima because of its ability to focus on larger scale structure while the pixel-based parameterization makes improvements locally by adding finer scale branches to the geometry.

7.1.3. Convergence Plots. The convergence of the methods is plotted for the heat conduction and MBB problems in Figure 8. Since the use of the word iteration in the context of optimization is somewhat ambiguous, we plot the compliance against the number of objective function value calls for the process. For the ADAM and MMA optimizers, the ratio of function and gradient calls is 1:1. To compare the SIMP and LS methods against each other, we bias the SIMP method using the optimized structures converted LS once again. The bias is computed as the difference between the SIMP method final objective value using the interpolated material and the SIMP

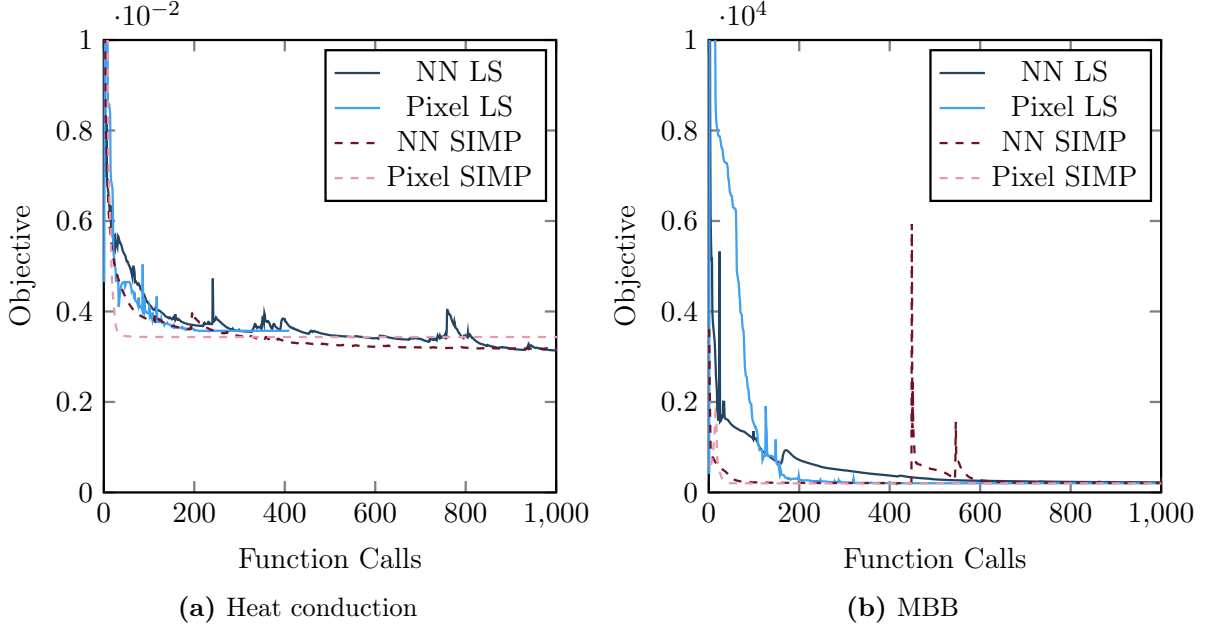


Figure 8. Convergence plot comparison for the benchmark problems. The objective value at each objective function call is plotted.

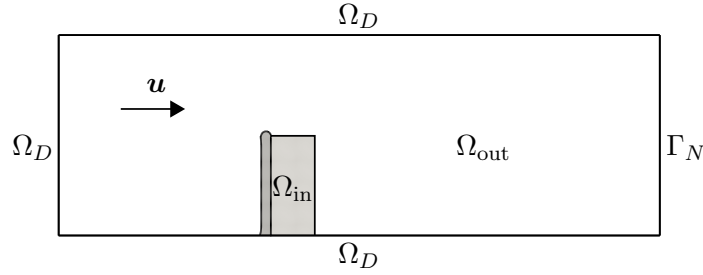


Figure 9. The beam support problem setup. An inlet velocity is prescribed on the left side, a homogenous Dirichlet condition on the top and bottom walls and a homogenous Neumann condition on the right wall Ω_N . The design region supporting the beam in light grey can be either fluid or solid. The solid domain Ω_{in} is composed of the dark grey beam and the solid part of the design region. The fluid region Ω_{out} is composed of the remainder of the channel, including the non-solid part of the design region.

method final objective value using the converted LS. This bias is applied to all of the series data in Figures 8 for the SIMP methods.

For the heat conduction problem in Figure 8a, the pixel-SIMP method converges the fastest, albeit to an inferior solution. The rest of the methods converge at similar rates. For the MBB problem in Figure 8b, the SIMP methods converge much faster than the LS methods although the NN-SIMP method jumps out of the minimum at later iterations and stabilizes later on.

7.2. Beam Support Design. The design of a beam support in a fluid channel is optimized in this section with the setup in [64]. The goal is to demonstrate the generality of the method which is shown here by its capacity to solve a multiphysics problem with complex boundary conditions. Density methods do not extend naturally to handle such problems and are faced with difficulty in obtaining accurate coupling between the fluid and structure since the representation of the interface is spread across cells in the vicinity of the boundary.

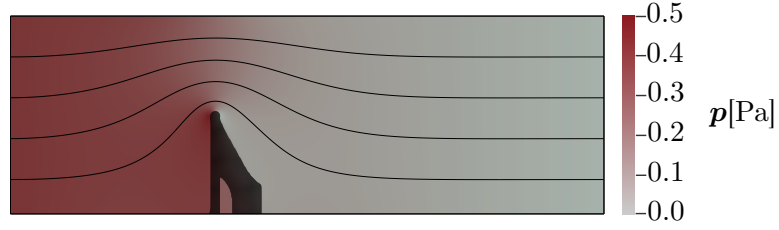


Figure 10. Optimized geometry for the beam support problem. Streamlines are plotted to represent the velocity field and pressure is indicated in the legend.

The problem setup is seen in Figure 9. For this problem, we set the fluid parameters as $\mu = 1m^2s^{-1}$ and $\alpha_u = 2.5\mu/0.01^2$ and use a parabolic velocity profile on the inlet with an average velocity of $0.01ms^{-1}$. For the structural parameters, we set $E = 1Pa$ and $\nu = 0.3$ and use a 0.45 volume fraction. We use the same network as in the poisson problem but set $w = (12, 12, 24, 46, 96, 96)$ and $l = (24, 24, 48, 96, 192, 192)$. The optimized geometry for problem is seen in Figure 10.

8. CONCLUSION

Here we propose a neural LS method as a means of coupling convolutional NNs and the unfitted LS method. The neural parameterization provides more regular geometries and similar, in some cases better, performance compared to the well known SIMP method of TO and the pixel-based counterpart LS method. The neural parameterization learns features at multiple scales during the optimization allowing for the emergence of regular structures whilst maintaining performance. The method takes longer to converge than the SIMP method and may not be suitable for simple problems such as those in linear elasticity. In this case, the network can be used in conjunction with the SIMP method. In contrast to SIMP, however, the method extends naturally to interface multiphysics problems and is more suitable in the general case. It should be noted that in our approach, the expressivity of geometries for the neural parameterization is the same as pixel counterpart methods since we use the same space V_h^1 in all cases to describe the geometry. A direction for development in the future would be to relax this constraint and also allow for the NN to control the space in which it expresses itself, potentially allowing for more efficient expressions of better topologies. Further investigation into architecture design and optimization strategy may also lead to a greater and more general improvement in performance.

9. REPLICATION OF RESULTS

All the codes being used in this paper are distributed as open source software. For reproducibility purposes, the implementation of the proposed TO methodology as well as the drivers being used to compare the different numerical methods are publicly available in the following repository: <https://github.com/ConnorMallon/NLSTO>

ACKNOWLEDGEMENTS

This research was partially funded by the Australian Government through the Australian Research Council (project number DP220103160).

CONFLICT OF INTEREST

On behalf of all authors, the corresponding author states that there is no conflict of interest.

REFERENCES

- [1] M. P. Bendsøe. “Optimal shape design as a material distribution problem”. In: *Structural Optimization* 1.4 (Dec. 1989), pp. 193–202. DOI: [10.1007/bf01650949](https://doi.org/10.1007/bf01650949).
- [2] O. Sigmund and K. Maute. “Topology optimization approaches”. In: *Structural and Multidisciplinary Optimization* 48.6 (Aug. 2013), pp. 1031–1055. DOI: [10.1007/s00158-013-0978-6](https://doi.org/10.1007/s00158-013-0978-6).

- [3] X. Guo and G.-D. Cheng. “Recent development in structural design and optimization”. In: *Acta Mechanica Sinica* 26.6 (Dec. 2010), pp. 807–823. DOI: [10.1007/s10409-010-0395-7](https://doi.org/10.1007/s10409-010-0395-7).
- [4] O. Sigmund. “A 99 line topology optimization code written in Matlab”. In: *Structural and Multidisciplinary Optimization* 21.2 (Apr. 2001), pp. 120–127. DOI: [10.1007/s001580050176](https://doi.org/10.1007/s001580050176).
- [5] G. H. Yoon. “Stress-based topology optimization method for steady-state fluid–structure interaction problems”. In: *Computer Methods in Applied Mechanics and Engineering* 278 (Aug. 2014), pp. 499–523. DOI: [10.1016/j.cma.2014.05.021](https://doi.org/10.1016/j.cma.2014.05.021).
- [6] S. Osher and J. A. Sethian. “Fronts propagating with curvature-dependent speed: Algorithms based on Hamilton-Jacobi formulations”. In: *Journal of Computational Physics* 79.1 (Nov. 1988), pp. 12–49. DOI: [10.1016/0021-9991\(88\)90002-2](https://doi.org/10.1016/0021-9991(88)90002-2).
- [7] J. A. Sethian. *Level set methods and fast marching methods : evolving interfaces in computational geometry, fluid mechanics, computer vision, and materials science*. eng. Cambridge, 1999.
- [8] N. P. van Dijk, K. Maute, M. Langelaar, and F. van Keulen. “Level-set methods for structural topology optimization: a review”. In: *Structural and Multidisciplinary Optimization* 48.3 (Mar. 2013), pp. 437–472. DOI: [10.1007/s00158-013-0912-y](https://doi.org/10.1007/s00158-013-0912-y).
- [9] S. J. Osher and F. Santosa. “Level Set Methods for Optimization Problems Involving Geometry and Constraints”. In: *Journal of Computational Physics* 171.1 (July 2001), pp. 272–288. DOI: [10.1006/jcph.2001.6789](https://doi.org/10.1006/jcph.2001.6789).
- [10] E. Burman, D. Elfverson, P. Hansbo, M. G. Larson, and K. Larsson. “Shape optimization using the cut finite element method”. In: *Computer Methods in Applied Mechanics and Engineering* 328 (Jan. 2018), pp. 242–261. DOI: [10.1016/j.cma.2017.09.005](https://doi.org/10.1016/j.cma.2017.09.005).
- [11] S.-H. Ha and S. Cho. “Level set based topological shape optimization of geometrically nonlinear structures using unstructured mesh”. In: *Computers & Structures* 86.13-14 (July 2008), pp. 1447–1455. DOI: [10.1016/j.compstruc.2007.05.025](https://doi.org/10.1016/j.compstruc.2007.05.025).
- [12] S. Yamasaki, T. Nomura, A. Kawamoto, K. Sato, and S. Nishiwaki. “A level set-based topology optimization method targeting metallic waveguide design problems”. In: *International Journal for Numerical Methods in Engineering* 87.9 (Feb. 2011), pp. 844–868. DOI: [10.1002/nme.3135](https://doi.org/10.1002/nme.3135).
- [13] G. Allaire, F. Jouve, and A.-M. Toader. “Structural optimization using sensitivity analysis and a level-set method”. In: *Journal of Computational Physics* 194.1 (Feb. 2004), pp. 363–393. DOI: [10.1016/j.jcp.2003.09.032](https://doi.org/10.1016/j.jcp.2003.09.032).
- [14] M. Y. Wang, X. Wang, and D. Guo. “A level set method for structural topology optimization”. In: *Computer Methods in Applied Mechanics and Engineering* 192.1-2 (Jan. 2003), pp. 227–246. DOI: [10.1016/s0045-7825\(02\)00559-5](https://doi.org/10.1016/s0045-7825(02)00559-5).
- [15] F. Dugast, Y. Favenec, and C. Josset. “Reactive fluid flow topology optimization with the multi-relaxation time lattice Boltzmann method and a level-set function”. In: *Journal of Computational Physics* 409 (May 2020), p. 109252. DOI: [10.1016/j.jcp.2020.109252](https://doi.org/10.1016/j.jcp.2020.109252).
- [16] J. Parvizian, A. Düster, and E. Rank. “Topology optimization using the finite cell method”. In: *Optimization and Engineering* 13.1 (July 2011), pp. 57–78. DOI: [10.1007/s11081-011-9159-x](https://doi.org/10.1007/s11081-011-9159-x).
- [17] E. Burman, P. Hansbo, M. G. Larson, and S. Zahedi. “Cut finite element methods for coupled bulk–surface problems”. In: *Numerische Mathematik* 133.2 (July 2015), pp. 203–231. DOI: [10.1007/s00211-015-0744-3](https://doi.org/10.1007/s00211-015-0744-3).
- [18] S. Badia, A. F. Martin, and F. Verdugo. “Mixed Aggregated Finite Element Methods for the Unfitted Discretization of the Stokes Problem”. In: *SIAM Journal on Scientific Computing* 40.6 (Jan. 2018), B1541–B1576. DOI: [10.1137/18M1185624](https://doi.org/10.1137/18M1185624).
- [19] S. Kreissl and K. Maute. “Levelset based fluid topology optimization using the extended finite element method”. In: *Structural and Multidisciplinary Optimization* 46.3 (Mar. 2012), pp. 311–326. DOI: [10.1007/s00158-012-0782-8](https://doi.org/10.1007/s00158-012-0782-8).
- [20] C. H. Villanueva and K. Maute. “CutFEM topology optimization of 3D laminar incompressible flow problems”. In: *Computer Methods in Applied Mechanics and Engineering* 320 (June 2017), pp. 444–473. DOI: [10.1016/j.cma.2017.03.007](https://doi.org/10.1016/j.cma.2017.03.007).

- [21] E. Burman. “Ghost penalty”. In: *Comptes Rendus Mathématique* 348.21-22 (Nov. 2010), pp. 1217–1220. DOI: [10.1016/j.crma.2010.10.006](https://doi.org/10.1016/j.crma.2010.10.006).
- [22] S. Badia, F. Verdugo, and A. F. Martín. “The aggregated unfitted finite element method for elliptic problems”. In: *Computer Methods in Applied Mechanics and Engineering* 336 (July 2018), pp. 533–553. DOI: [10.1016/j.cma.2018.03.022](https://doi.org/10.1016/j.cma.2018.03.022). arXiv: [1709.09122](https://arxiv.org/abs/1709.09122).
- [23] S. Badia, E. Neiva, and F. Verdugo. “Linking ghost penalty and aggregated unfitted methods”. In: *Computer Methods in Applied Mechanics and Engineering* 388 (Jan. 2022), p. 114232. DOI: [10.1016/j.cma.2021.114232](https://doi.org/10.1016/j.cma.2021.114232).
- [24] S. Badia, E. Neiva, and F. Verdugo. “Robust high-order unfitted finite elements by interpolation-based discrete extension”. In: *Computers & Mathematics with Applications* 127 (Dec. 2022), pp. 105–126. DOI: [10.1016/j.camwa.2022.09.027](https://doi.org/10.1016/j.camwa.2022.09.027).
- [25] S. Kreissl, G. Pingen, and K. Maute. “An explicit level set approach for generalized shape optimization of fluids with the lattice Boltzmann method”. In: *International Journal for Numerical Methods in Fluids* 65.5 (Jan. 2011), pp. 496–519. DOI: [10.1002/flid.2193](https://doi.org/10.1002/flid.2193).
- [26] N. Dijk, M. Langelaar, and F. Keulen. “Explicit level-set-based topology optimization using an exact Heaviside function and consistent sensitivity analysis”. In: *International Journal for Numerical Methods in Engineering* 91.1 (May 2012), pp. 67–97. DOI: [10.1002/nme.4258](https://doi.org/10.1002/nme.4258).
- [27] H. Adeli and H. S. Park. “A neural dynamics model for structural optimization—Theory”. In: *Computers & Structures* 57.3 (Nov. 1995), pp. 383–390. DOI: [10.1016/0045-7949\(95\)00048-1](https://doi.org/10.1016/0045-7949(95)00048-1).
- [28] Z. Zhang et al. “TONR: An exploration for a novel way combining neural network with topology optimization”. In: *Computer Methods in Applied Mechanics and Engineering* 386 (Dec. 2021), p. 114083. DOI: [10.1016/j.cma.2021.114083](https://doi.org/10.1016/j.cma.2021.114083).
- [29] R. V. Woldseth, N. Aage, J. A. Bærentzen, and O. Sigmund. *On the use of Artificial Neural Networks in Topology Optimisation*. 2022. DOI: [10.48550/ARXIV.2208.02563](https://doi.org/10.48550/ARXIV.2208.02563).
- [30] V.-N. Hoang, N.-L. Nguyen, D. Q. Tran, Q.-V. Vu, and H. Nguyen-Xuan. “Data-driven geometry-based topology optimization”. In: *Structural and Multidisciplinary Optimization* 65.2 (Jan. 2022). DOI: [10.1007/s00158-022-03170-8](https://doi.org/10.1007/s00158-022-03170-8).
- [31] Y. Yu, T. Hur, J. Jung, and I. G. Jang. “Deep learning for determining a near-optimal topological design without any iteration”. In: *Structural and Multidisciplinary Optimization* 59.3 (Oct. 2018), pp. 787–799. DOI: [10.1007/s00158-018-2101-5](https://doi.org/10.1007/s00158-018-2101-5).
- [32] B. Li, C. Huang, X. Li, S. Zheng, and J. Hong. “Non-iterative structural topology optimization using deep learning”. In: *Computer-Aided Design* 115 (Oct. 2019), pp. 172–180. DOI: [10.1016/j.cad.2019.05.038](https://doi.org/10.1016/j.cad.2019.05.038).
- [33] S. Zheng, Z. He, and H. Liu. “Generating three-dimensional structural topologies via a U-Net convolutional neural network”. In: *Thin-Walled Structures* 159 (Feb. 2021), p. 107263. DOI: [10.1016/j.tws.2020.107263](https://doi.org/10.1016/j.tws.2020.107263).
- [34] N. A. Kallioras, G. Kazakis, and N. D. Lagaros. “Accelerated topology optimization by means of deep learning”. In: *Structural and Multidisciplinary Optimization* 62.3 (Mar. 2020), pp. 1185–1212. DOI: [10.1007/s00158-020-02545-z](https://doi.org/10.1007/s00158-020-02545-z).
- [35] Y. Joo, Y. Yu, and I. G. Jang. “Unit Module-Based Convergence Acceleration for Topology Optimization Using the Spatiotemporal Deep Neural Network”. In: *IEEE Access* 9 (2021), pp. 149766–149779. DOI: [10.1109/access.2021.3125014](https://doi.org/10.1109/access.2021.3125014).
- [36] H. Deng and A. C. To. “Topology optimization based on deep representation learning (DRL) for compliance and stress-constrained design”. In: *Computational Mechanics* 66.2 (May 2020), pp. 449–469. DOI: [10.1007/s00466-020-01859-5](https://doi.org/10.1007/s00466-020-01859-5).
- [37] A. Chandrasekhar and K. Suresh. “TOuNN: Topology Optimization using Neural Networks”. In: *Structural and Multidisciplinary Optimization* 63.3 (Nov. 2020), pp. 1135–1149. DOI: [10.1007/s00158-020-02748-4](https://doi.org/10.1007/s00158-020-02748-4).
- [38] S. Hoyer, J. Sohl-Dickstein, and S. Greydanus. *Neural reparameterization improves structural optimization*. 2019. eprint: [arXiv:1909.04240](https://arxiv.org/abs/1909.04240).
- [39] A. R. Barron. “Approximation and estimation bounds for artificial neural networks”. In: *Machine Learning* 14.1 (Jan. 1994), pp. 115–133. DOI: [10.1007/bf00993164](https://doi.org/10.1007/bf00993164).

- [40] O. Ronneberger, P. Fischer, and T. Brox. *U-Net: Convolutional Networks for Biomedical Image Segmentation*. 2015. arXiv: [1505.04597](https://arxiv.org/abs/1505.04597) [cs.CV].
- [41] D. Ulyanov, A. Vedaldi, and V. Lempitsky. “Deep Image Prior”. In: 128.7 (Mar. 2020), pp. 1867–1888. DOI: [10.1007/s11263-020-01303-4](https://doi.org/10.1007/s11263-020-01303-4).
- [42] J. Bezanson, A. Edelman, S. Karpinski, and V. B. Shah. “Julia: A fresh approach to numerical computing”. In: *SIAM Review* 59.1 (2017), pp. 65–98. DOI: [10.1137/141000671](https://doi.org/10.1137/141000671).
- [43] S. Badia and F. Verdugo. “Gridap: An extensible Finite Element toolbox in Julia”. In: *Journal of Open Source Software* 5.52 (2020), p. 2520. DOI: [10.21105/joss.02520](https://doi.org/10.21105/joss.02520).
- [44] F. Verdugo and S. Badia. “The software design of Gridap: A Finite Element package based on the Julia JIT compiler”. In: *Computer Physics Communications* 276 (July 2022), p. 108341. DOI: [10.1016/j.cpc.2022.108341](https://doi.org/10.1016/j.cpc.2022.108341).
- [45] M. Innes et al. “Fashionable Modelling with Flux”. In: *CoRR* abs/1811.01457 (2018). arXiv: [1811.01457](https://arxiv.org/abs/1811.01457).
- [46] H. Deng and A. C. To. “A Parametric Level Set Method for Topology Optimization Based on Deep Neural Network”. In: *Journal of Mechanical Design* 143.9 (Mar. 2021). DOI: [10.1115/1.4050105](https://doi.org/10.1115/1.4050105).
- [47] D. RUMELHART, G. HINTON, and R. WILLIAMS. “Learning Internal Representations by Error Propagation”. In: *Readings in Cognitive Science*. Elsevier, 1988, pp. 399–421. DOI: [10.1016/b978-1-4832-1446-7.50035-2](https://doi.org/10.1016/b978-1-4832-1446-7.50035-2).
- [48] J. L. Barrera, M. J. Geiss, and K. Maute. “Hole seeding in level set topology optimization via density fields”. In: *Structural and Multidisciplinary Optimization* 61.4 (Feb. 2020), pp. 1319–1343. DOI: [10.1007/s00158-019-02480-8](https://doi.org/10.1007/s00158-019-02480-8).
- [49] X. Xing, P. Wei, and M. Y. Wang. “A finite element-based level set method for structural optimization”. In: *International Journal for Numerical Methods in Engineering* 82.7 (Nov. 2009), pp. 805–842. DOI: [10.1002/nme.2785](https://doi.org/10.1002/nme.2785).
- [50] S. Badia, F. Verdugo, and A. F. Martín. “The aggregated unfitted finite element method for elliptic problems”. In: *Computer Methods in Applied Mechanics and Engineering* 336 (July 2018), pp. 533–553. DOI: [10.1016/j.cma.2018.03.022](https://doi.org/10.1016/j.cma.2018.03.022).
- [51] S. Badia, P. A. Martorell, and F. Verdugo. “Geometrical discretisations for unfitted finite elements on explicit boundary representations”. In: *Journal of Computational Physics* 460 (July 2022), p. 111162. DOI: [10.1016/j.jcp.2022.111162](https://doi.org/10.1016/j.jcp.2022.111162).
- [52] F. de Prenter, C. Verhoosel, G. van Zwieten, and E. van Brummelen. “Condition number analysis and preconditioning of the finite cell method”. In: *Computer Methods in Applied Mechanics and Engineering* 316 (Apr. 2017), pp. 297–327. DOI: [10.1016/j.cma.2016.07.006](https://doi.org/10.1016/j.cma.2016.07.006).
- [53] J. Parvizian, A. Düster, and E. Rank. “Finite cell method”. In: *Computational Mechanics* 41.1 (Apr. 2007), pp. 121–133. DOI: [10.1007/s00466-007-0173-y](https://doi.org/10.1007/s00466-007-0173-y).
- [54] T. Borrvall and J. Petersson. “Topology optimization of fluids in Stokes flow”. In: *International Journal for Numerical Methods in Fluids* 41.1 (2002), pp. 77–107. DOI: [10.1002/flid.426](https://doi.org/10.1002/flid.426).
- [55] G. Allaire, C. Dapogny, and F. Jouve. “Shape and topology optimization”. In: *Geometric Partial Differential Equations - Part II*. Elsevier, 2021, pp. 1–132. DOI: [10.1016/bs.hna.2020.10.004](https://doi.org/10.1016/bs.hna.2020.10.004).
- [56] A. Sharma, H. Villanueva, and K. Maute. “On shape sensitivities with heaviside-enriched XFEM”. In: *Structural and Multidisciplinary Optimization* 55.2 (Dec. 2016), pp. 385–408. DOI: [10.1007/s00158-016-1640-x](https://doi.org/10.1007/s00158-016-1640-x).
- [57] E. Burman, S. Claus, P. Hansbo, M. G. Larson, and A. Massing. “CutFEM: Discretizing geometry and partial differential equations”. In: *International Journal for Numerical Methods in Engineering* 104.7 (2015), pp. 472–501. DOI: [10.1002/nme.4823](https://doi.org/10.1002/nme.4823). eprint: <https://onlinelibrary.wiley.com/doi/pdf/10.1002/nme.4823>.
- [58] C. Lang, D. Makhija, A. Doostan, and K. Maute. “A simple and efficient preconditioning scheme for heaviside enriched XFEM”. In: *Computational Mechanics* 54.5 (Aug. 2014), pp. 1357–1374. DOI: [10.1007/s00466-014-1063-8](https://doi.org/10.1007/s00466-014-1063-8).

- [59] F. Verdugo and S. Badia. “The software design of Gridap: a Finite Element package based on the Julia JIT compiler”. In: (2021). DOI: [10.48550/ARXIV.2109.12818](https://doi.org/10.48550/ARXIV.2109.12818).
- [60] J. Revels, M. Lubin, and T. Papamarkou. *Forward-Mode Automatic Differentiation in Julia*. 2016. DOI: [10.48550/ARXIV.1607.07892](https://doi.org/10.48550/ARXIV.1607.07892).
- [61] K. Svanberg. “The method of moving asymptotes—a new method for structural optimization”. In: *International Journal for Numerical Methods in Engineering* 24.2 (Feb. 1987), pp. 359–373. DOI: [10.1002/nme.1620240207](https://doi.org/10.1002/nme.1620240207).
- [62] D. P. Kingma and J. Ba. *Adam: A Method for Stochastic Optimization*. 2014. DOI: [10.48550/ARXIV.1412.6980](https://doi.org/10.48550/ARXIV.1412.6980).
- [63] A. Gersborg-Hansen, M. P. Bendsøe, and O. Sigmund. “Topology optimization of heat conduction problems using the finite volume method”. In: *Structural and Multidisciplinary Optimization* 31.4 (Mar. 2006), pp. 251–259. DOI: [10.1007/s00158-005-0584-3](https://doi.org/10.1007/s00158-005-0584-3).
- [64] N. Jenkins and K. Maute. “An immersed boundary approach for shape and topology optimization of stationary fluid-structure interaction problems”. In: *Structural and Multidisciplinary Optimization* 54.5 (May 2016), pp. 1191–1208. DOI: [10.1007/s00158-016-1467-5](https://doi.org/10.1007/s00158-016-1467-5).